ELSEVIER

A numerical method for simulating concentrated rigid particle suspensions in an elongational flow using a fixed grid

G. D'Avino [a], P.L. Maffettone [a], M.A. Hulsen [b,*], G.W.M. Peters [b]

[a] *Dipartimento di Ingegneria Chimica, Universitá di Napoli Federico II, Napoli I-80125, Italy*
[b] *Department of Mechanical Engineering, Eindhoven University of Technology, Eindhoven 5600 MB, The Netherlands*

Abstract

In this work a new numerical method for concentrated inertialess rigid particle suspensions in a planar elongational flow using a fixed mesh is presented. The main concept is to randomly relocate a particle on an inflow section of the domain when it crosses the outflow boundaries. A three-layer domain is considered in order to: (i) develop a small computational domain as the representative sample of the whole suspension, (ii) impose the elongational flow boundary conditions far from the particles, (iii) achieve a steady state (in a statistical meaning). Our scheme uses a time-independent fixed grid avoiding the difficulties involved in deforming meshes and remeshing of the domain. In this way, computations can proceed indefinitely and micro-structural fluctuations around a steady state can be studied.

A fictitious domain is implemented in order to easily manage the rigid-body motion. The particles are described by their boundaries only (rigid-ring description) and the rigid-body motion is imposed through Lagrange multipliers. The bulk properties are recovered by using an averaging procedure where the traction forces on the particle surface are recovered by the Lagrange multipliers.

The scheme has been combined with a standard velocity–pressure finite element formulation and 2D simulations of a large number (150 and 225) of particles in a Newtonian medium are performed. Local as well as bulk properties are evaluated and discussed. The results show very good agreement with dilute theory as well as with other numerical simulations in the literature for higher concentrations.

Our formulation is well suited for viscoelastic suspensions and can be easily extended to 3D simulations.
© 2007 Elsevier Inc. All rights reserved.

Keywords: Direct numerical simulation; Concentrated suspensions; Fictitious domain; Rigid-ring description; Suspension rheology; Elongational flow; Finite element method

* Corresponding author.
  E-mail addresses: gadavino@unina.it (G. D'Avino), pierluca.maffettone@unina.it (P.L. Maffettone), m.a.hulsen@tue.nl (M.A. Hulsen), g.w.m.peters@tue.nl (G.W.M. Peters).

1. Introduction

In the last decades, direct numerical simulations (DNSs) techniques have been developed in order to predict and understand the complex flow of particle-filled fluids. The motion of the fluid is governed by the (Navier–)Stokes equations and the motion of the particles by the linear and angular momentum equations of rigid-body dynamics. The coupling of the fluid and the particles is achieved through the no-slip condition on the particle boundaries and the hydrodynamic forces and torques on the particles. The hydrodynamic forces and torques are, of course, those arising from the computed motion of the fluid, and therefore are not known in advance. It has to be pointed out that no approximation for these forces and torques is made. So, in DNS methods, hydrodynamic interactions are not modeled but computed.

An increasing interest in rigid particle suspensions can be observed. Typically, in all systems of practical interest, the concentration of particles is high so they are non-dilute or concentrated. In other words, a many-particle system should be considered and the hydrodynamic interactions play a crucial role by affecting the local flow fields, bulk properties and the final behavior of the material.

In order to manage the problem computationally, we need to develop a suited simulation scheme that uses the smallest domain that still has the same average properties as the whole suspension. Hence, by solving the flow problem in this domain, we are able to predict the average micro-structure and the bulk properties of the suspensions, with reduced CPU time and memory.

This idea has been used by Hwang et al. [1,2] where the authors combine Lees–Edwards boundary conditions, i.e. a sliding bi-periodic domain, with a standard velocity–pressure finite element formulation for a Newtonian suspension as well as a DEVSS/DG (discrete elastic viscous split stress/discontinuous Galerkin) scheme for viscoelastic suspensions in simple shear flow. According to this scheme, each frame slides relatively to one another by an amount determined by a given shear rate. So, a frame can be considered as a sample of the whole suspension and transforms the many-particle suspension into a single unit cell.

Recently, the bi-periodic frame concept has been extended to planar extensional flow [3]. However, in order to deal with such a flow, a deformation in time of the bi-periodic frame is proposed. As a consequence, after a certain time, the frames cannot be deformed anymore since the smallest characteristic length of the frame is comparable with the characteristic dimension of the particles. Hence, it is difficult to achieve a steady state for this imposed flow field. This is especially true for a viscoelastic fluid at high Weissenberg number, where large strains are needed before a steady state is obtained. Finally, in the scheme described in [3] remeshing of the domain is also done in order to keep the aspect ratio of the elements close to one.

In this work, we propose a new simulation scheme that circumvents these problems. The main concept is to relocate a particle on the inflow boundary of the domain when it crosses the outflow sections. So, no periodic boundary condition is imposed. In particular, the computational domain is divided into three concentric square regions: in the internal one the particles move, the micro-structural and bulk properties are evaluated in this region. So, this region can be considered as a sample of the whole suspension. In the intermediate region the particles can move as well and, when they cross the outflow boundaries of that region, they are relocated randomly on one of the two inflow sections of the same region. Finally, the outer region only contains fluid since particles cannot enter. The elongational flow boundary conditions are imposed on the external boundaries of the outer region: so the particles feel the presence of the elongational flow boundary conditions only as an imposed 'far field'.

According to this scheme, no deformation of the domain occurs and a time-independent fixed grid can be used (and no remeshing of the domain is needed). Furthermore, an average steady state can be achieved: we do not need to stop the simulation since the domain dimensions do not change. Finally, this scheme is suited for the simulation of viscoelastic suspensions. Indeed, after the relocation of the particles in the intermediate region, the stress has time to develop before particles enter the internal region where the properties are calculated.

In this work, we consider a concentrated suspension of rigid, non-Brownian disks in a planar elongational flow, where the particle and fluid inertia can be neglected. Indeed, a vast literature is based on the inertialess assumption (see for example the method of Stokesian dynamics [4] for concentrated suspensions in Newtonian fluids). Our final goal is to compare the results for a Newtonian suspension with the ones where the suspending

fluid is a melt and can be represented by a viscoelastic model having a very high viscosity. So, the Newtonian suspensions under investigation are characterized by a high viscosity as well and therefore the inertialess assumption is appropriate here.

The analysis is carried out for a Newtonian medium. The particle–fluid interactions are taken into account by implementing a Lagrange multiplier/fictitious domain method (LM/FDM) [5,6]. The force-free, torque-free rigid body motion of the particles is described by a rigid-ring problem [1,2]. So, a fixed mesh is used for the computation and the particles are described by their boundaries only, through collocation points. This description is possible because inertia is neglected. Finally, the rigid-body motion constraints are imposed through Lagrange multipliers that can be identified as traction forces on the particle surfaces (with a correction due to the fluid stress inside the object).

Another difference with the works of Hwang et al. [1–3] is that with our scheme a particle is not splitted into parts since it never crosses the boundary of the whole domain. However, since a particle can cross the sample internal region, a slight modification of the bulk stress formula is required.

We limit the simulations to two dimensions in order to show the feasibility of the new method based on a fixed grid. Therefore, the simulations only represent the planar elongational flow of fluids filled with particles having a long aspect ratio, such as fibers, which are aligned normal to the plane of flow. For more general flows, like spherical particle suspensions, we need to extend the method to three dimensions. This will be part of future research and will require iterative solvers and parallel calculations.

Numerical simulations are performed and the local flow fields are presented for a many-particle problem. The bulk stress is recovered by using a standard averaging procedure [7]. Finally, the bulk rheological properties are discussed and a comparison with the results of Hwang and Hulsen [3] is carried out. Our results on the bulk viscosity of the suspension are in very good agreement. Moreover, an anisotropic structure is also found even if no transient behavior as in [3] is observed.

The paper is organized as follows: in Section 2, the problem definition is presented. The governing equations for fluid, particles and hydrodynamic interactions are given as well. In Section 3, the weak form for the whole domain is derived. Moreover, the spatial implementation and time integration algorithms are discussed. In Section 4, the bulk stress formula is given. In Section 5, the method is validated. A comparison between the Lagrange multipliers/fictitious domain method and a boundary fitted method is carried out. A simple test problem is chosen. In particular, local flow fields and bulk stress are exploited. The influence of the number of collocation points on the accuracy of the solution is also analyzed. Moreover, the relationship between Lagrange multipliers and traction forces on the particles is discussed. In Section 6, the simulation procedure is introduced. The computational scheme is presented and particle area fraction and bulk stress formulas are given. In Section 7, the results for planar extensional flow are presented. A many-particle problem (150 and 225 particles) is simulated. Local velocity, pressure, stress fields are analyzed and discussed, by means of snapshots of the simulations. Finally, bulk properties (stress tensor and viscosity) are evaluated.

2. Modeling

Suspensions consisting of a large number of rigid non-Brownian circular disk particles (2D problem) in planar elongational flow are considered. A schematic representation of the problem is shown in Fig. 1: many particles (circles) move in a Newtonian fluid medium. Particles are denoted by $P_i(t)$, $i = 1, \ldots, N$, where N is the total number of particles in the domain.

A square domain, denoted by Ω, is considered. On the fluid boundaries, denoted by Γ_i, $i = 1, \ldots, 4$, planar elongational flow boundary conditions are imposed. The Cartesian x and y coordinates are selected such that the origin is at the center of the domain. The particles move according to the imposed flow and hydrodynamic interactions: their rigid-body motion is completely defined by the translational velocity, $\boldsymbol{U}_i = (U_i, V_i)$, and angular velocity, $\boldsymbol{\omega}_i = \omega_i \boldsymbol{k}$, where $\boldsymbol{k}$ is the unit vector in the direction normal to the x–y plane. Moreover, for a particle P_i, $\boldsymbol{X}_i = (X_i, Y_i)$, $\boldsymbol{\Theta}_i = \Theta_i \boldsymbol{k}$ are used for the coordinates of the particle center and the angular rotation, respectively. Here, the governing equations for a Newtonian suspension are presented, for the fluid domain as well as for the particles.
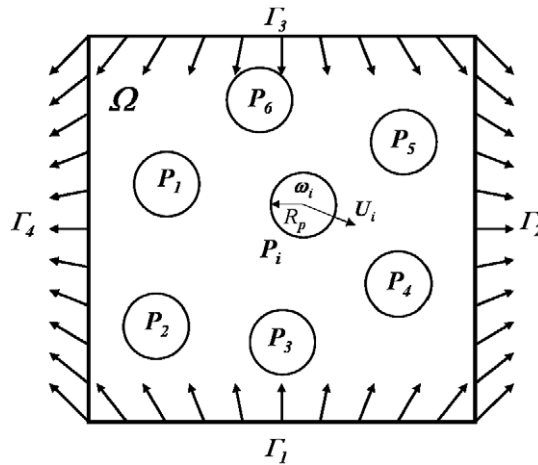
Fig. 1. Schematic representation of the problem: a square fluid domain (Ω) filled with many particles ($P_i(t)$) is considered. Elongational flow conditions on the fluid boundaries (Γ_i) are imposed.

2.1. Fluid domain

For a Newtonian and inertialess fluid, the momentum balance, the continuity and the constitutive relation are:

$$\nabla \cdot \boldsymbol{\sigma} = \mathbf{0} \quad \text{in } \Omega \setminus P(t), \tag{1}$$

$$\nabla \cdot \boldsymbol{u} = 0 \quad \text{in } \Omega \setminus P(t), \tag{2}$$

$$\boldsymbol{\sigma} = -p\boldsymbol{I} + 2\eta\boldsymbol{D} \quad \text{in } \Omega \setminus P(t), \tag{3}$$

where $\boldsymbol{u}$, $\boldsymbol{\sigma}$, p, $\boldsymbol{I}$, $\boldsymbol{D}$ and η are the velocity, the stress, the pressure, the 2×2 unity tensor, the rate-of-deformation tensor and the viscosity, respectively and $P = \cup P_i$.

The fluid boundary conditions are given by:

$$\boldsymbol{u} = \boldsymbol{U}_i + \boldsymbol{\omega}_i \times (\mathbf{x} - \boldsymbol{X}_i) \quad \text{on } \partial P_i(t) \quad (i = 1, \ldots, N), \tag{4}$$

$$u = \dot{\epsilon}x, \quad v = -\dot{\epsilon}y \quad \text{on } \Gamma_i \quad (i = 1, \ldots, 4) \tag{5}$$

assuming that all particles are fully immersed in the fluid. Eq. (4) is the rigid-body condition and $\boldsymbol{x}$ are the coordinates of the points on the particle surface. Eq. (5) gives the planar elongational flow boundary conditions where $\dot{\epsilon}$ is the elongational rate. In the absence of inertia, no initial conditions are needed for the velocity field of the fluid as well as for the particles. Finally, it is sufficient to set the pressure level in one point of the domain.

2.2. Particle domain

Following [1,2], in this work a rigid-ring description for the particle domain is used. In this way, a particle is considered as a rigid ring which is filled with the same fluid as in the fluid domain. This description can be used if the inertia is neglected. So, it is necessary to discretize only the particle boundary, which leads to reduction in memory requirements and simplifies the implementation. Moreover, as shown later, the traction force on the particle boundaries can be obtained as a part of the solution, when the rigid-body constraints are implemented through Lagrange multipliers.

With the rigid-ring description, the equations for a particle P_i can be written as:

$$\nabla \cdot \hat{\boldsymbol{\sigma}} = \mathbf{0} \quad \text{in } P_i(t), \tag{6}$$

$$\nabla \cdot \boldsymbol{u} = 0 \quad \text{in } P_i(t), \tag{7}$$

$$\hat{\boldsymbol{\sigma}} = -p\boldsymbol{I} + 2\eta\boldsymbol{D} \quad \text{in } P_i(t), \tag{8}$$

$$\boldsymbol{u} = \boldsymbol{U}_i + \boldsymbol{\omega}_i \times (\boldsymbol{x} - \boldsymbol{X}_i) \quad \text{on } \partial P_i(t). \tag{9}$$

Again, Eqs. (6)–(9) are equations for the momentum balance, the continuity, the constitutive relation and the boundary condition, respectively, which are the same for the fluid domain. Note that we have denoted the fluid stress tensor inside the particle ($\hat{\boldsymbol{\sigma}}$) different from the stress tensor in the fluid between particles in order to make a distinction between the stress tensor inside the 'real' rigid particle ($\boldsymbol{\sigma}$) and the fictitious fluid stress. The solution of the problem inside a particle is the rigid-body motion itself as applied on the particle boundary [1,2]:

$$\boldsymbol{u} = \boldsymbol{U}_i + \boldsymbol{\omega}_i \times (\boldsymbol{x} - \boldsymbol{X}_i) \quad \text{in } P_i(t). \tag{10}$$

With this description, the pressure level inside a particle is undetermined/not unique, in theory. However it turns out that, in the numerical implementation with the fictitious domain method, it is not necessary to specify the pressure level inside the particle directly. Finally, the movement of particles is given by the following kinematic equations:

$$\frac{\mathrm{d}\boldsymbol{X}_i}{\mathrm{d}t} = \boldsymbol{U}_i, \quad \boldsymbol{X}_i|_{t=0} = \boldsymbol{X}_{i,0}, \tag{11}$$

$$\frac{\mathrm{d}\boldsymbol{\Theta}_i}{\mathrm{d}t} = \boldsymbol{\omega}_i, \quad \boldsymbol{\Theta}_i|_{t=0} = \boldsymbol{\Theta}_{i,0}. \tag{12}$$

Eq. (12) is completely decoupled from the other equations for circular particles.

2.3. Hydrodynamic interactions

Eq. (4) (and (9) as well) adds (for the 2D case) three additional unknowns for each particle, namely the translational and angular velocities of the particle. So, it is necessary to consider the balance equations for drag forces and torques, acting on the particle boundaries. Under the assumptions of absence of inertia and external forces and torques, the particles are force-free and torque-free, so the balance equations are given by:

$$\boldsymbol{F}_i = \int_{\partial P_i(t)} \boldsymbol{\sigma} \cdot \boldsymbol{n} \, \mathrm{d}s = \mathbf{0}, \tag{13}$$

$$\boldsymbol{T}_i = \int_{\partial P_i(t)} (\boldsymbol{x} - \boldsymbol{X}_i) \times (\boldsymbol{\sigma} \cdot \boldsymbol{n}) \, \mathrm{d}s = \mathbf{0}. \tag{14}$$

In these equations, $\boldsymbol{F}_i = (F_{i,x}, F_{i,y})$ and $\boldsymbol{T}_i = T_i\boldsymbol{k}$ are the total force and torque on the particle boundaries, $\boldsymbol{n}$ is the outwardly directed unit normal vector on ∂P_i. As we can see, for the 2D case, (13) and (14) add three equations to the system.

Eqs. (1)–(3) for the fluid domain with boundary conditions (4) and (5), the corresponding equations for the particle domain (6)–(8) with boundary condition (9) and the hydrodynamic equations (13) and (14) form a system in the unknowns: p, $\boldsymbol{u}$, $\boldsymbol{\sigma}$, $\boldsymbol{U}_i$, $\boldsymbol{\omega}_i$. The kinematic equations (11) and (12) are integrated to update the particle positions and rotations. So, every time-step the problem is solved and the flow fields, rigid-body unknowns and stresses are evaluated. Next, we need to find an expression for the evaluation of bulk rheological properties (bulk stress, bulk viscosity, etc.). This will be presented in Section 4.

3. Weak form and implementation

3.1. Weak form

In this section the derivation of the weak form is presented. In deriving the weak form of the governing equations, the hydrodynamic forces and torques on the particles can be completely eliminated by combining

the fluid and particle equations of motion into a single weak equation of motion for the combined fluid and particle system. This equation is called the combined equation of motion and can be obtained by choosing a suitable variational space for the velocity which incorporates the rigid-body motion constraint (see [5,8] for details). This formulation has two important advantages: the first is that the hydrodynamic forces and torques do not have to be computed or modeled anymore since they cancel in the weak form. The second advantage is that these schemes are not subject to numerical instabilities as shown in [8].

Extending the combined equation of motion to cover the particle domain, removing the rigid-ring constraint from the variational spaces and enforce it as a constraint using the Lagrange multipliers, the weak form for the whole domain can be obtained:

Find $\boldsymbol{u} \in H^1(\Omega)^2$, $\boldsymbol{U}_i \in \Re^2$, $\boldsymbol{\omega}_i \in \Re$, $\boldsymbol{\lambda}_i \in L^2(\partial P_i(t))$, $p \in L^2(\Omega)$ $(i = 1, \ldots, N)$ such that:

$$-\int_\Omega \nabla \cdot \boldsymbol{v} p \, \mathrm{d}A + \int_\Omega 2\eta \boldsymbol{D}(\boldsymbol{v}) : \boldsymbol{D}(\boldsymbol{u}) \, \mathrm{d}A + \sum_{i=1}^{N} \langle \boldsymbol{v} - (\boldsymbol{V}_i + \boldsymbol{\chi}_i \times (\boldsymbol{x} - \boldsymbol{X}_i)), \boldsymbol{\lambda}_i \rangle_{\partial P_i} = \boldsymbol{0}, \tag{15}$$

$$\int_\Omega q \nabla \cdot \boldsymbol{u} A = 0, \tag{16}$$

$$\langle \boldsymbol{\mu}_i, \boldsymbol{u} - (\boldsymbol{U}_i + \boldsymbol{\omega}_i \times (\boldsymbol{x} - \boldsymbol{X}_i)) \rangle_{\partial P_i} = \boldsymbol{0} \tag{17}$$

for all $\boldsymbol{v} \in H^1(\Omega)^2$, $\boldsymbol{V}_i \in \Re^2$, $\boldsymbol{\chi}_i \in \Re$, $\boldsymbol{\mu}_i \in L^2(\partial P_i(t))$, $q \in L^2(\Omega)$ $(i = 1, \ldots, N)$.

This weak form is at the basis of the fictitious domain method since it includes both the fluid and particle domain. The rigid-body condition is included in the momentum balance and the constraints are implemented through Lagrange multipliers, only on the particle boundaries. As a consequence, a fixed, time-independent, very simple mesh can be used, circumventing the necessity of remeshing and projection, as needed in the ALE method [9–11].

The solution of Eqs. (15)–(17) gives $(\boldsymbol{u}, p, \boldsymbol{U}_i, \boldsymbol{\omega}_i)$ as well as all the Lagrangian multipliers. Then, the particle positions and rotations can be updated by integrating the kinematic equations (Eqs. (11) and (12)) and the problem is solved at the next time step. As previously discussed, it is not necessary to specify initial conditions for $\boldsymbol{u}$, $\boldsymbol{U}_i$ and $\boldsymbol{\omega}_i$ since both fluid and particles are inertialess. Instead, it is mandatory to set the pressure level, for example by specifying the pressure in a point of the domain. The resulting system is linear in the state variables and symmetric. It is solved by a direct method based on a sparse multi-frontal variant of Gaussian elimination (HSL/MA57) [12]. However, a direct method can be used only for 2D simulations. For 3D flows iterative solvers will be needed to lower the memory requirements.

3.2. Spatial discretization

The fictitious domain allows to use a very simple, time-independent mesh for the discretization of the whole domain. In this work, a rectangular regular mesh with bi-quadratic interpolation for the velocity and bi-linear continuous interpolation for the pressure is used ($Q_2 - Q_1$ elements). It is well known that this kind of element satisfies the LBB condition. Due to the discontinuity of the pressure field between the fluid and particle domain a discontinuous interpolation for the pressure should preferably be used [1,2,13]. However, as we will discuss later, even if we use a discontinuous pressure interpolation ($Q_2 - P_1^d$ element), the pressure value on the particle surface cannot be recovered accurately.

From the rigid-ring description, the particles are discretized by their boundaries. The weak form of the rigid-ring description (Eq. (17)) has been approximated by point collocation:

$$\langle \boldsymbol{\mu}_i, \boldsymbol{u} - (\boldsymbol{U}_i + \boldsymbol{\omega}_i \times (\boldsymbol{x} - \boldsymbol{X}_i)) \rangle_{\partial P_i} \approx \sum_{k=1}^{N_c} \boldsymbol{\mu}_{i,k} \cdot \{\boldsymbol{u}(\boldsymbol{x}_k) - (\boldsymbol{U}_i + \boldsymbol{\omega}_i \times (\boldsymbol{x}_k - \boldsymbol{X}_i)), \tag{18}$$

where N_c is the number of collocation points on the particle surface, $\boldsymbol{x}_k$ are the coordinates of the kth collocation point and $\boldsymbol{\mu}_{i,k}$ the corresponding Lagrange multiplier. This boundary discretization is very simple to implement and, as shown in Section 5, stresslets on the particles can be recovered by Lagrange multipliers values. It is important to point out that the number of collocation points is crucial for the accuracy of the bulk stress: too few points cannot represent adequately the rigid-body motion while too many collocation points

lead to an overestimation of the surface stress integrals. A detailed analysis about the choice of N_c will be carried out in Section 5.

In Fig. 2 a comparison between a typical unstructured mesh for a boundary fitted method (on the left), and the fictitious domain mesh for the same particle configuration (on the right) is shown. In the first case only the fluid domain is discretized: no solution is obtained inside the particles. In the fictitious domain, however, we can observe a mesh inside the objects as well. As a consequence, after solving the equations, pressure and velocity (and stress) are also evaluated in the nodes inside the particles. Although it is not possible to accurately recover the pressure (and stresses) on the particle surface (see Section 5), a simple regular mesh can be used, giving the opportunity to solve very complex interaction problems in a simple way. Also, the discretization of the particle boundaries through collocation points is shown in Fig. 2. Finally, in the same figure, a typical $Q_2 - Q_1$ element is shown.

3.3. Time integration

For a given initial particle configuration, Eqs. (15)–(17) can be solved and then it is possible to update the particle positions and rotations. To do this, it is necessary to integrate the kinematic equations (11) and (12). An explicit time integration scheme has been implemented: the Euler method at the first time step:

$$\boldsymbol{X}_i^{n+1} = \boldsymbol{X}_i^n + \Delta t \boldsymbol{U}_i^n \tag{19}$$

and the Adams–Bashforth method for the next time steps:

$$\boldsymbol{X}_i^{n+1} = \boldsymbol{X}_i^n + \Delta t \left(\frac{3}{2} \boldsymbol{U}_i^n - \frac{1}{2} \boldsymbol{U}_i^{n-1} \right). \tag{20}$$

4. Bulk stress

As previously discussed, we are interested in the rheological properties of concentrated suspensions in planar elongational flow, such as the stress tensor, viscosity, etc. The flow and stress fields obtained from the equations just presented are local. Local values of pressure and velocity give information about the stress distribution around the particles and thus also about the hydrodynamic interaction between particles. However, it is also important to evaluate global properties (bulk properties) in order to make predictions about global behavior of such materials. To do this, we have to consider a bulk stress expression related to local quantities. We will consider the Batchelor formula [7]. The bulk stress tensor can be calculated as the sum of the fluid contribution and the particle contribution, as follows (for the 2D case):

$$\langle \boldsymbol{\sigma} \rangle = \frac{1}{A} \int_A \boldsymbol{\sigma} \, \mathrm{d}A = \frac{1}{A} \int_{A_f} \boldsymbol{\sigma} \, \mathrm{d}A + \frac{1}{A} \int_{\partial A_p} \boldsymbol{\sigma} \cdot \boldsymbol{n}\boldsymbol{x} \, \mathrm{d}s, \tag{21}$$

where $\langle \cdot \rangle$ is an area average quantity in an area A, A_f is the area occupied by the fluid and ∂A_p is the total particle surface. For the Newtonian constitutive equation (Eq. (3)), the bulk stress can be written as:
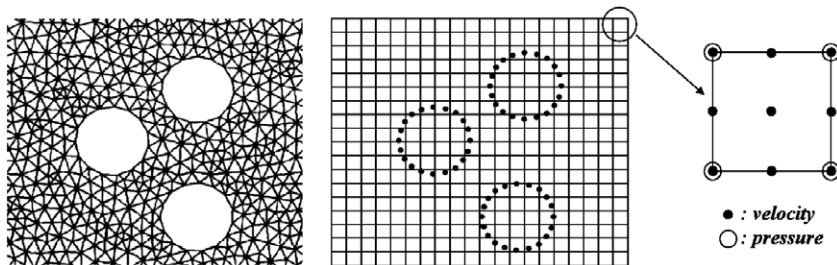

Fig. 2. Comparison between an unstructured mesh (left) and a fictitious domain (right). In the fictitious domain method the particles are described by their boundaries through collocation points (rigid-ring description). A typical $Q_2 - Q_1$ element is shown as well.

$$\langle \boldsymbol{\sigma} \rangle = \langle \boldsymbol{\sigma} \rangle_{\mathrm{f}} + \frac{1}{A} \int_{\partial A_{\mathrm{p}}} \boldsymbol{t} \boldsymbol{x} \, \mathrm{d}s = -\langle p \rangle_{\mathrm{f}} \boldsymbol{I} + 2\eta \langle \boldsymbol{D} \rangle + \frac{1}{A} \int_{\partial A_{\mathrm{p}}} \boldsymbol{t} \boldsymbol{x} \, \mathrm{d}s, \tag{22}$$

where $\boldsymbol{t}$ is the traction force on the particle surface and $\langle \cdot \rangle_{\mathrm{f}} = 1/A \int_{A_{\mathrm{f}}} \cdot \, \mathrm{d}A$ is a weighted area average quantity in A_{f}. Of course, $\langle \boldsymbol{D} \rangle = \langle \boldsymbol{D} \rangle_{\mathrm{f}}$ because the rate-of-deformation tensor is zero inside the particle domain. In Eq. (22) the first two terms of the right-hand side represent the fluid contribution and the third term is the contribution of all particles.

We need the stress tensor on the particle boundaries in order to calculate the integral term in Eq. (22). However, as shown in the next section, the fictitious domain method cannot accurately evaluate the stress on the particle boundaries due to the discontinuity of the pressure and velocity gradients at the particle boundaries. This problem is circumvented by considering the relation between the Lagrange multipliers and traction forces on the boundary of a particle. For a rigid-ring description, it has been shown [1] that the Lagrange multipliers are related to the traction force on the boundary plus the stress contribution of the fluid inside the rigid ring:

$$\int_{\partial A_{\mathrm{p}}} \boldsymbol{t} \boldsymbol{x} \, \mathrm{d}s = \langle \boldsymbol{\lambda}, \boldsymbol{x} \rangle + \int_{A_{\mathrm{p}}} \hat{\boldsymbol{\sigma}} \, \mathrm{d}A, \tag{23}$$

where:

$$\int_{A_{\mathrm{p}}} \hat{\boldsymbol{\sigma}} \, \mathrm{d}A = -\int_{A_{\mathrm{p}}} p \, \mathrm{d}A \boldsymbol{I} + \int_{A_{\mathrm{p}}} 2\eta \boldsymbol{D} \, \mathrm{d}A. \tag{24}$$

Note that, in theory, the fluid inside the rigid ring moves like a rigid body and that $\boldsymbol{D} = \boldsymbol{0}$ inside the rigid ring. In the numerical implementation this is only approximately true. However, the contribution of the rate-of-deformation tensor can still be neglected (see Section 5) and only the pressure contribution has to be calculated by performing an integration on the particle domain. By combining Eqs. (22) and (23), we can calculate the bulk stress as follows:

$$\langle \boldsymbol{\sigma} \rangle = \langle \hat{\boldsymbol{\sigma}} \rangle + \frac{1}{A} \langle \boldsymbol{\lambda}, \boldsymbol{x} \rangle, \tag{25}$$

where $\langle \hat{\boldsymbol{\sigma}} \rangle$ is the average over the full domain (fluid + particles) of the fluid stress tensor (we extended the definition of $\hat{\boldsymbol{\sigma}}$ with $\hat{\boldsymbol{\sigma}} = \boldsymbol{\sigma}$ in the region between the particles).

The fluid contribution to the bulk stress can be recovered as follows:

$$\langle \boldsymbol{\sigma} \rangle_{\mathrm{f}} = \langle \hat{\boldsymbol{\sigma}} \rangle - \frac{1}{A} \int_{A_{\mathrm{p}}} \hat{\boldsymbol{\sigma}} \, \mathrm{d}A, \tag{26}$$

whereas the particle contribution in Eq. (22) can be computed using Eq. (23). It should be noticed that if one is interested in the bulk stress, it is not necessary to evaluate the integral of fluid stress inside the particles. Instead, if one needs the fluid and particle contribution separately, the integral of fluid stress tensor inside the objects is required.

Finally, it is important to point out that Eq. (25) is valid only if the particles are completely immersed in the computational domain. In our simulation scheme, the particles cross the boundaries of the domain where the bulk properties are computed also. Therefore, a slightly change in the area A will be made, as shown in Section 6.

5. Code validation

5.1. Local fields

The code has been validated through a comparison with a boundary fitted method (BFM) using a commercial code (*PolyFlow©*). First, pressure and velocity fields have been investigated. A simple system as test problem is chosen: a single particle is collocated at the center of a square domain; on the sides of the square planar elongational boundary conditions are imposed ($\dot{\epsilon} = 0.5$) and a unit viscosity is chosen. The radius of the particle is chosen equal to 0.05 and the square side is 20 times this radius ($R_{\mathrm{p}} = 0.05$, $L_x = L_y = 1.0$). In order to

preserve the symmetry of the problem, the particle does not move or rotate, so the no-slip boundary conditions on the particle surface for BFM are $u = v = 0$. Of course, the fictitious domain method (FDM) does not need to specify particle boundary conditions because the no-slip conditions are imposed through Lagrange multipliers on the collocation points. A very fine triangular mesh is used in the BFM, finer close to the particle where larger gradients are expected (typical element size close to the particle is 0.005, i.e. 10 times smaller than the particle radius). A regular square mesh for FDM is used. The side of the square element is chosen 1/100 the square domain so a 100×100 grid is considered. The particle surface is discretized by 28 collocation points, chosen equally distributed on the particle boundary. This choice corresponds approximately to one point per element. As shown later, this distribution of collocation points is the optimal choice for this particle radius/element dimension ratio. The pressure is set to zero in the bottom-left corner of the square domain. Finally, a quadratic interpolation for the velocity and linear continuous interpolation for the pressure is chosen for BFM. The steady state problem is solved by means of BFM and FDM and pressure and velocity fields are compared.

In Fig. 3, the pressure and velocity behavior along the positive x-axis is shown. First of all, notice that the FDM solution has field values also inside the particle. The velocity magnitude predicted by FDM (open circles) matches the BFM one (solid line). Moreover, FDM predicts a zero-value for the velocity inside the particle (the particle does not move), as expected. The results are different for the pressure field. Both methods predict a pressure value near zero far from the particle (of course the set pressure level on the external fluid boundaries is expected). Approaching the particle, a monotonically decreasing behavior is predicted by the BFM solution that matches the FDM solution up to a small distance from the particle surface (≈ 0.01). The BFM solution shows a minimum value on the particle surface whereas for the FDM case the pressure increases slightly. It has to be pointed out that: (i) a different value of pressure is predicted on the particle boundary and (ii) the pressure inside the particle is not constant (and is not zero everywhere).

This different behavior can be justified by considering that the pressure is discontinuous across the particle boundary. The BFM "doesn't see" this discontinuity since only the fluid domain is considered; the interior of the particle is not a part of the solution. Instead, in the FDM, the particle domain is discretized as well and, to take into account the discontinuity, a very fine mesh close to the particle surface is required. Indeed, since the interpolating functions are continuous inside an element, a finer mesh can reduce the distance where the pressure goes from the minimum to zero value. However, the pressure value on the surface cannot be predicted as accurately as a BFM. Of course, the stress tensor is affected by the same problem, since it has a pressure contribution (see Eq. (3)). As a consequence, the bulk stress cannot be accurately evaluated using Eq. (21) (or (22)) but we will use Eq. (25) where only the stress over the total domain and the Lagrange multipliers are required.
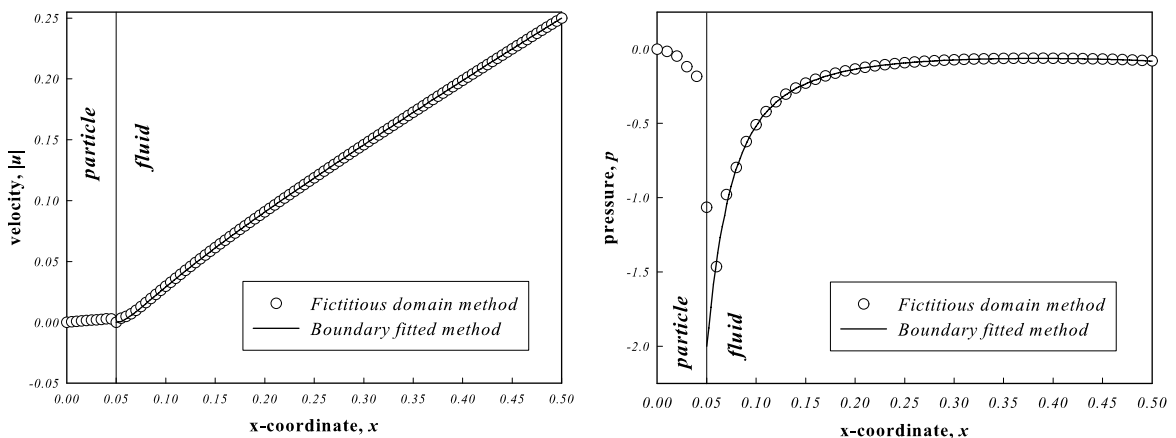

Fig. 3. Velocity (left) and pressure (right) field on the positive x-axis, as predicted by the boundary fitted method (solid line) and a fictitious domain method (open circles).

A discontinuous interpolation for the pressure has also been implemented ($Q_2 - P_1^d$ element). The results (not presented) show the same behavior: the pressure predicted by the FDM follows the BFM one up to a very close distance from the particle boundary, then goes up. Therefore, a discontinuous interpolation for the pressure is not able to predict the value of pressure on the particle boundary either, since, the pressure is discontinuous between the elements but continuous inside an element. In this work, a continuous interpolation is used.

5.2. Bulk stress

For the rigid-ring description, only the boundaries of the particle domain need to be discretized. The rigid-body motion is enforced through Lagrange multipliers, by means of collocation points. Moreover, we can recover the bulk stress of the suspension from the Lagrange multipliers, as stated in the previous section.

In this subsection, we show that the number of collocation points is crucial for the accuracy of the bulk stress tensor. Of course, by fixing the number of collocation points, the orientation of the collocation point grid on the particle boundaries should not affect the bulk stress value. We will show this as well. Again, the same test problem is considered.

In Fig. 4, the xx-component (full circles) and the absolute values of the yy-component (open circles) of the bulk stress versus the number of collocation points (N_c) are shown for a fluid viscosity $\eta = 1$. The straight line is the value of the bulk stress obtained by a boundary fitted method. On the left, the results for a 50×50 grid are plotted. On the right, a twice finer grid is considered. In both cases, the trend is upwards. A small number of points leads to an underestimation of the bulk stress. On the other hand, after using a large number points an overestimated stress value is obtained. Moreover, after a critical N_c value, the bulk stress does not increase anymore. Note that the fluid contribution to the bulk stress has a value of 1. The particle contribution is much smaller but since the error can mostly be attributed to the error in the particle contribution, the error for a large number of points is approximately 6% and 2% in the 50×50 and 100×100 grid, respectively. An optimal value of N_c, say $N_{c,opt}$, exists ($N_{c,opt} \cong 15$ for a 50×50 mesh, $N_{c,opt} \cong 28$ for a 100×100 mesh), where the error is minimal. These optimal values correspond to about one collocation point for each element, in agreement with Hwang et al. [1,2]. Of course, $N_{c,opt}$ depends on the grid resolution as well as on the dimensions of the particles. Since we will change the radius of the particles, a preliminary analysis on the optimal choice of N_c is carried out. For each radius exploited we solve the test problem for different N_c and we compare the results with the bulk stress from the BFM. Then, $N_{c,opt}$ is evaluated and the number of the collocation points of the particles in the suspension is set equal to $N_{c,opt}$.
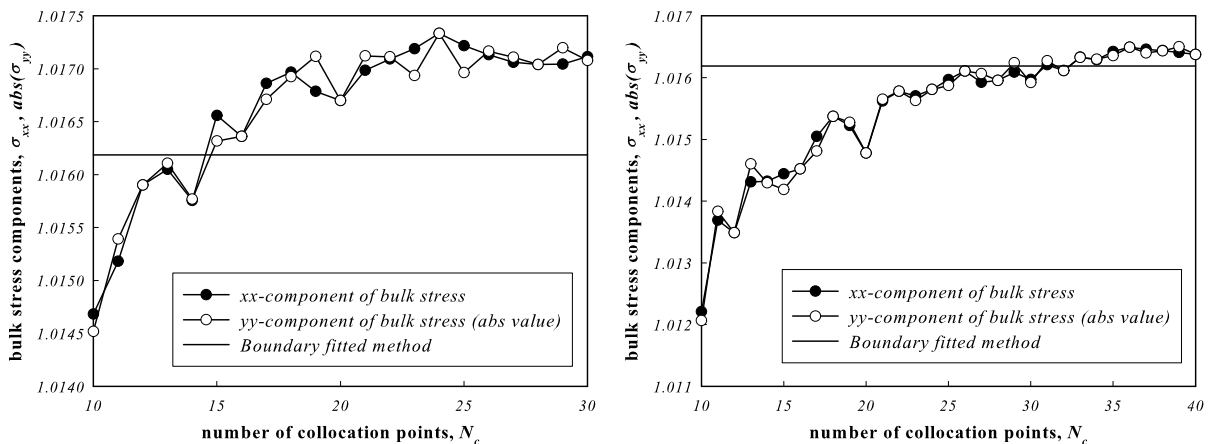

Fig. 4. Bulk stress as a function of the number of collocation points for 50×50 (on the left) and 100×100 (on the right) grid. The close circles refer to the xx-component whereas with the open circles the absolute value of the yy-component is depicted. The straight line is the BFM prediction.

Next, we check whether the bulk stress is independent of the orientation of the collocation point grid. Let us consider again the simple test problem of one particle at the center of the domain, with the same parameters but with 30 collocation points instead of 28. Initially, we choose equally distributed points starting from the top of the particle (see Fig. 5, left). The steady state problem is solved and the bulk stress is calculated as stated in Eq. (25). The same problem is solved, but this time the collocation points are rotated by an angle θ with respect to the previous configuration, as shown in Fig. 5, right. This procedure is repeated for many θ and the results are plotted in Fig. 6 (full circles represent the xx-component of the bulk stress whereas open circles are the absolute value of the yy-component). The phase shift angle θ ranges in $I_\theta = [0, \pi/15]$ since, for $N_c = 30$ and for different θ, the same configurations can be recovered. The straight line is the bulk stress calculated by the boundary fitted method. We can see that the quantities plotted are nearly independent of the rotation of the collocation point grid and they match the bulk stress evaluated by means of the BFM. So, the orientation of the grid does not affect the bulk stress. Although in our simulations we use $\theta = 0$, the results show that the accuracy of the bulk stress is not related to the specific symmetry of the collocation points with respect to the fluid mesh. This also indicates that the collocation method can be easily extended to non-circular particles, where the orientation of the collocation points cannot be fixed.

5.3. Fluid and particle contribution to the bulk stress

A validation of Eqs. (23) and (26) for recovering the particle and fluid contribution is carried out. By performing the procedure previously discussed, the traction force term (from Eq. (23) divided by the area A) and $\langle \boldsymbol{\sigma} \rangle_f$ (from Eq. (26)) are plotted as a function of θ in Fig. 7 (with the same meaning of the symbols as in Fig. 6). Notice that in both integrals the contribution of $\langle \boldsymbol{\sigma} \rangle$ inside the particle is taken into account. Again, the quantities plotted are nearly independent of the rotation of the collocation points grid and they match the fluid and particle contribution to the bulk stress evaluated by means of the BFM.

Finally, the integral of the pressure inside the particle (divided by the area A) as a function of θ is shown in Fig. 8. A Monte Carlo integration has been used, as the Gaussian quadrature formula is difficult to implement. The integral of $\boldsymbol{D}$ has also been evaluated and it is about 10^{-5}, for every θ. The values are not small compared to the particle contribution. They also depend on the angle θ, which stresses the fact that the fluid pressure inside the particle has a numerical origin. Hence, we conclude that the internal stress integral (Eq. (24)) is not small and fully dominated by the pressure term. As a consequence, the $\boldsymbol{D}$ term can be neglected.

In conclusion, the fluid and particle contribution to the bulk stress can be evaluated using Eqs. (23) and (26) together with Eq. (23), where the integral of $\boldsymbol{D}$ inside the particle can be neglected. If only the total bulk stress is required, Eq. (25) can be used and no integration inside the particle is necessary.
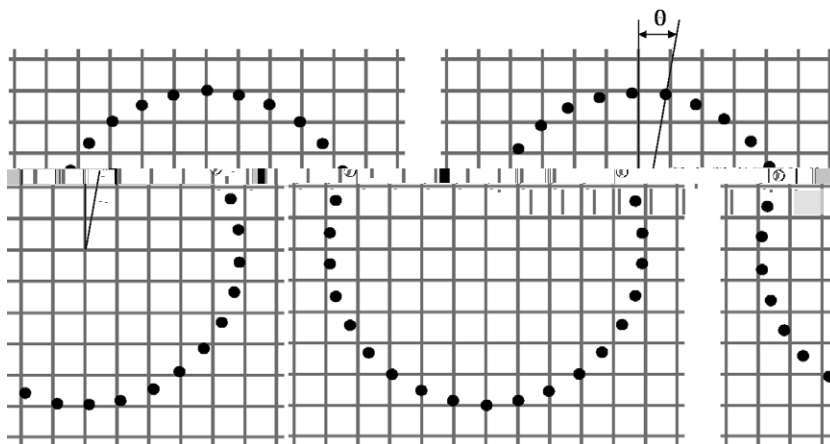

Fig. 5. Collocation point distribution on the boundary of a particle located at the center of the square domain. 30 equally distributed points are considered. On the left, the first collocation point lies on the highest point of the circle. On the right the same grid is rotated of $\theta = 10°$.

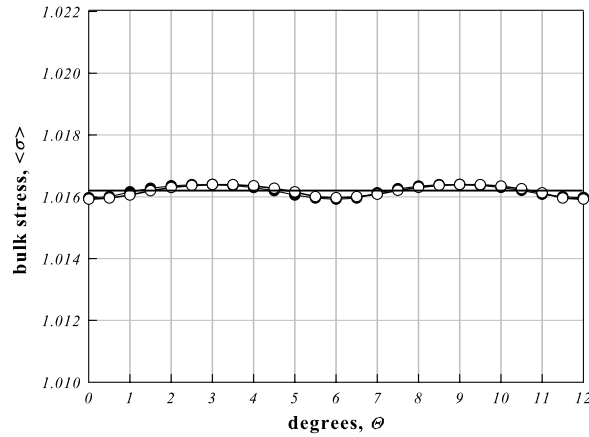Fig. 6. Bulk stress versus the phase shift angle. The close circles refer to the xx-component whereas with the open circles the absolute value of the yy-component is depicted.
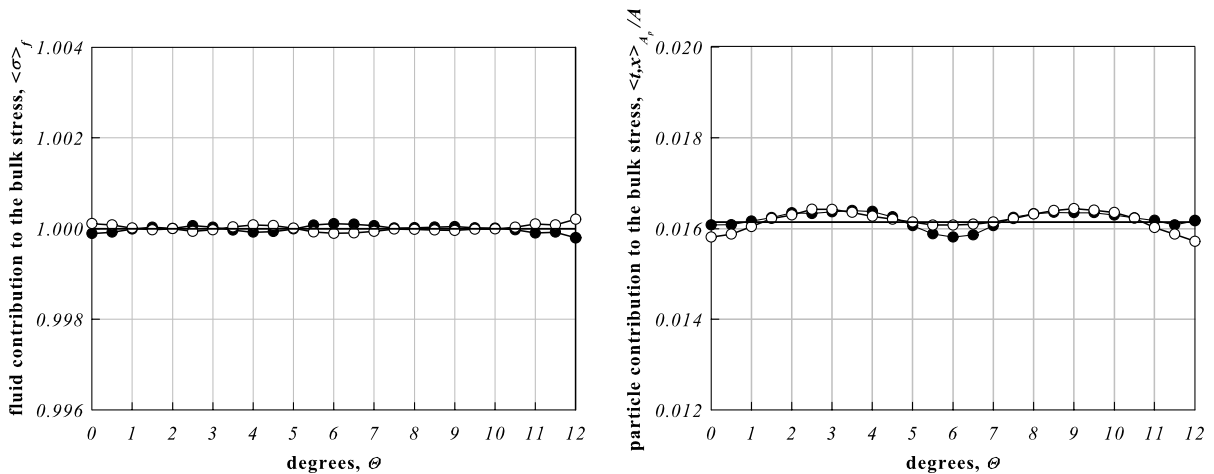

Fig. 7. Fluid (on the left) and particle (on the right) contributions to the bulk stress. These quantities have been obtained by using Eqs. (26) and (23) (divided by the area A), respectively. The close circles refer to the xx-component whereas with the open circles the absolute value of the yy-component is depicted.

6. Simulation procedure

6.1. Basics

In this section, the simulation procedure is presented. The basic idea is to simulate a computationally small domain that is able to describe the bulk properties of the suspension. For this purpose, (i) a sufficiently high number of particles is required and (ii) only the hydrodynamic interactions should influence the particles or, in other words, the particles should not feel the presence of the boundary conditions imposed on the external side of the square domain.

Let us consider an unfilled Newtonian fluid in a planar elongational flow, as depicted in Fig. 9. The typical streamlines are portrayed and two inflow and two outflow sections can be distinguished (see also Eq. (5)). Now, let us insert rigid particles inside the fluid. For simplicity, we will consider three particles only. The simulation procedure is schematized in Fig. 10.

In this picture, four time frames of the procedure are shown. Initially (first frame, $t = 0$), the particles are positioned randomly inside the fluid. Each time step the governing equations are solved, local fields can be
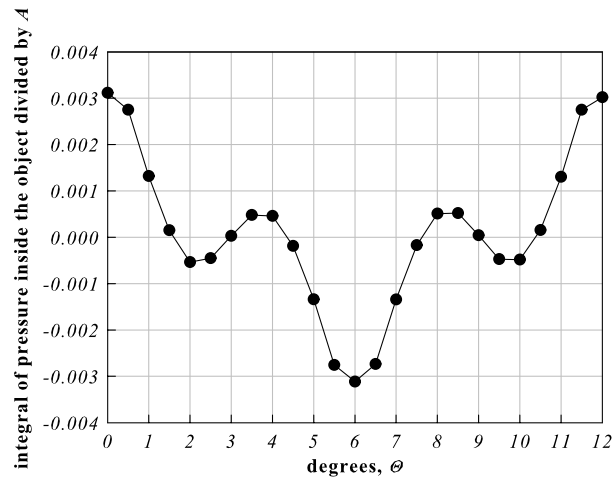
Fig. 8. Integral of the fluid pressure inside the particle (divided by the area A) versus the phase shift angle. A Monte Carlo integration has been used.

evaluated and the particle positions are updated. The particles will move according to the streamlines and the hydrodynamic interactions as well (second frame). In the next time step, the particles will change configuration again (third frame). Note that the particle number "2" is very close to the right boundary of the domain, so, in the next time step, it would partly go out. Then, in the next time step, the particle "2" is randomly relocated on one of the two inflow sections (fourth frame). It is important to point out that the inflow section is randomly chosen as well as the position of the particle on this section. After the relocation, the equations are solved again and the particle positions are updated as stated by the kinematic equations, and so on. When a particle is relocated, its position in the next time step cannot be updated using the Adams–Bashforth algorithm (Eq. (20)), since the velocity in the previous time step (before the relocation) is required. So, only for this step, the Euler method (Eq. (19)) is used.

A schematic representation of the computational domain used in our simulations is depicted in Fig. 11. Three different regions can be distinguished: an internal region (A-region), an intermediate region (B-region) and an external region (C-region).

In the A-region the particles can move and only in this region the bulk properties are evaluated. So, this region can be considered as a sample for the whole suspension.
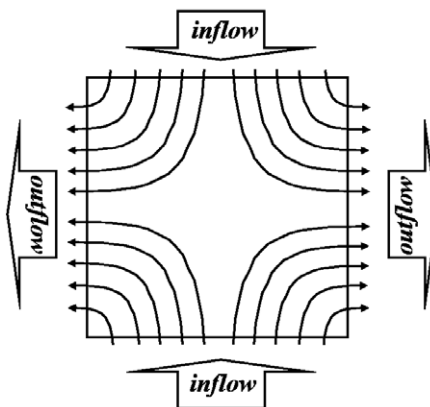

Fig. 9. Schematic representation of the streamlines for a unfilled Newtonian fluid in a planar elongational flow. Two inflow sections and two outflow sections can be distinguished.
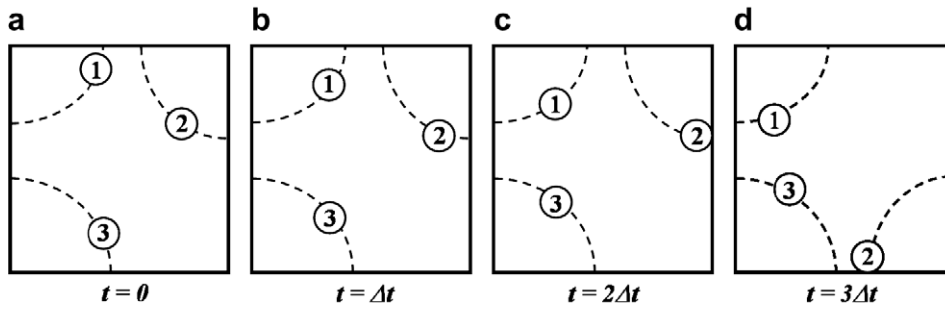
Fig. 10. Scheme of the simulation procedure: (a) initially, the particles are randomly distributed in the fluid; (b) the particles move according to the streamlines and hydrodynamic interactions; (c) the particle "2" is close to the boundary; (d) the particle "2" is randomly relocated on one of the two inflow sections.

In the *B*-region the particles can move as well and, when they cross the outflow boundaries of it, they are relocated randomly on one of the two inflow sections of the same region. Therefore, the particles in this region affect the particles in the sample *A*-region, as should be because the sample region should be surrounded by the remainder part of the suspension. Moreover, for viscoelastic simulations, this region is mandatory because the stress surrounding the particles, after the relocation, needs time to develop before the particles enter in the *A*-region in order to achieve a "developed" state (in a statistical meaning). However, viscoelasticity is not a topic in this paper.

The *C*-region is particle free, i.e., no particles can enter such region. This region is indeed necessary to avoid that particles can approach the elongational flow boundary condition, Eq. (5), which are imposed on the external boundaries of *C*-region. In the absence of the *C*-region strong fluctuations in the pressure field are observed that result from the incompatible rigid body motion of the particle and the imposed elongational boundary conditions. The width of *C*-region has to be chosen large enough with respect to particle radius to avoid these large artificial fluctuations.
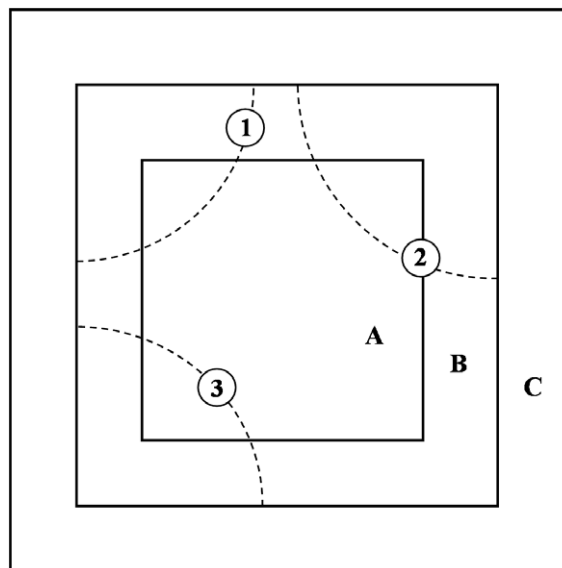

Fig. 11. Schematic representation of the computational domain. The particles can move in the *A*- and *B*-regions. Only in the *A*-region the bulk calculations are performed. When a particle crosses the outflow sections of the *B*-region, it is relocated on the inflow sections of the same region. The elongational flow conditions are imposed on the *C*-region external boundaries.

As explained below, the particle area fraction (ϕ) in the A-region for this scheme changes in time. Indeed, the number of particles in the A-region is not constant. Therefore, simulation of very dilute systems ($0.0 < \phi < 0.05$) must be performed sufficiently long in order to get accurate statistical averages.

6.2. Particle area fraction and bulk stress

All the calculations concerning particle area fraction, viscosity and bulk stresses are performed in the A-region of the computational domain, even if the particles can move in the middle region as well. So a situation where particles are partially inside the A-region can occur (see the particle "2" in Fig. 11).

As a consequence, the particle area fraction and bulk stress evaluations are not trivial. For each particle configuration (=each time step), the particle area fraction is calculated as follows:

$$\phi = \frac{\sum_{i=1}^{N_{\text{int}}} \pi R_{\text{p},i}^2 + \sum_{i=1}^{N_{\text{cross}}} A_{\text{c},i}}{A_{A\text{-region}}}. \tag{27}$$

The first summation refers to the particles that are completely inside the A-region and N_{int} is the number of these particles. The second summation takes into account the areas inside the A-region of the particles crossing this region (marked areas in Fig. 12). Therefore, in Eq. (27), N_{cross} is the number of the particles crossing the boundaries and $A_{\text{c},i}$ is the area inside the A-square of these particles. Finally, $A_{A\text{-region}}$ is the area of the A-region. The marked areas in Fig. 12 are evaluated by implementing geometric rules ($P_{\text{c},i-1}$ and $P_{\text{c},i}$ particles in the figure) or through a Monte Carlo integration if the particle crosses the corner of the A-region ($P_{\text{c},i+1}$ particle in the figure).

The bulk stress formula is slightly more complicated. The bulk stress expression, Eq. (25), is valid only if the particles are completely immersed in the domain. However, if a particle crosses the boundary of the domain where the bulk properties are evaluated (A-region), the contribution of the particle is the stress integral on the part of the particle domain that is inside this region. The 'real' stress inside a rigid particle is unknown and it is not possible to compute the stress contribution of such a particle. So, we have to modify the domain such that all particles are fully included in the domain, but the 'average' domain (in time and space) should still approximate the A-region.

Let us consider Fig. 13. The new computational domain is enclosed by the bold line: it is given by the A-domain plus the external part of the particles crossing the square boundaries and with the center inside the square (diagonal marked areas) minus the internal part of the particles crossing the square boundaries and with the center outside the square (square marked areas). So, a particle gives a contribution to the bulk stress only if it is completely inside the A-region or if it crosses the boundary of the A-region and has the center inside it. As a consequence, when a particle crosses the A-region inflow boundary, it will not give contribution until its center is inside this region and vice versa for the outflow boundary. In this way, on the average in time, the right contribution to the bulk stress of the particles crossing the A-region can be recovered.

According to this change, we can apply Eq. (25) to the new extended domain. So, the bulk stress formula can be written as:
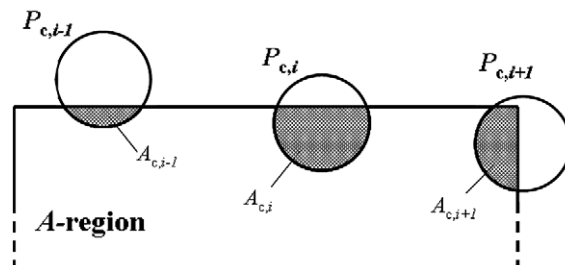

Fig. 12. Relative positions of the particles crossing the boundaries of the A-region. The summation of marked regions gives the particle area inside the square of these particles.

$$\langle \boldsymbol{\sigma} \rangle = \frac{\int_{A\text{-region}} \hat{\boldsymbol{\sigma}} \, \mathrm{d}A - \int_{\sum A_{\text{c-int}}} p \, \mathrm{d}A \boldsymbol{I} + \int_{\sum A_{\text{c-ext}}} p \, \mathrm{d}A \boldsymbol{I} + \sum_{i=1}^{N_{\text{int}}+N_{\text{c-int}}} \langle \boldsymbol{\lambda}, \boldsymbol{x} \rangle_i}{A_{A\text{-region}} + \sum_{i=1}^{N_{\text{c-int}}} A_{\text{c-int},i} - \sum_{i=1}^{N_{\text{c-ext}}} A_{\text{c-ext},i}}, \tag{28}$$

where $N_{\text{c-int}}$ and $N_{\text{c-ext}}$ are the number of particles crossing the boundaries with the center inside and outside the A-region, respectively; $A_{\text{c-int}}$ and $A_{\text{c-ext}}$ are the areas shown in Fig. 13. We have some remarks on Eq. (28): (i) the area of the extended domain is given by the denominator of the formula, (ii) $\langle \hat{\boldsymbol{\sigma}} \rangle$ is split into $\langle \hat{\boldsymbol{\sigma}} \rangle_{A\text{-region}} + \langle \hat{\boldsymbol{\sigma}} \rangle_{A_{\text{c-int}}} - \langle \hat{\boldsymbol{\sigma}} \rangle_{A_{\text{c-ext}}}$, (iii) the last two terms, i.e. $\langle \hat{\boldsymbol{\sigma}} \rangle_{A_{\text{c-int}}} - \langle \hat{\boldsymbol{\sigma}} \rangle_{A_{\text{c-ext}}}$, are approximated by using the pressure term only, similar to procedure for approximating Eq. (24).

To apply this formula, one needs to evaluate the integral of the pressure on $A_{\text{c-int}}$ and $A_{\text{c-ext}}$. This integral is calculated again by performing a Monte Carlo integration. For many particles, this method could be expensive in computational time. However, 10,000 random points are shown to be sufficient for a good accuracy.
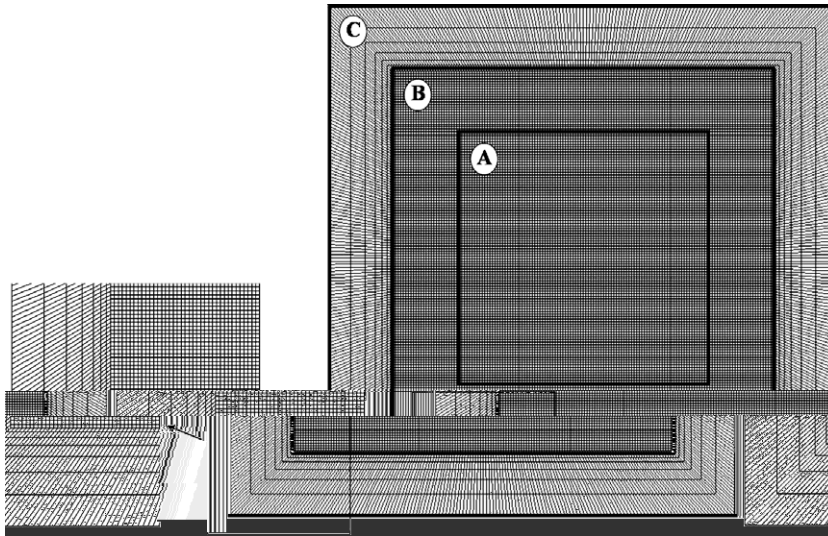
7. Results

Fig. 14. Mesh used in the simulations. *A*- and *B*-regions are discretized through a regular square mesh. A trapezoidal coarser mesh is used for *C*-region, since the particles cannot enter in this region.

Table 1
Mesh parameters

Symbol	Description	Value
$l_{x,A}$	Length of the *A*-region in the *x*-direction	1.0
$l_{y,A}$	Length of the *A*-region in the *y*-direction	1.0
$n_{x,A}$	Number of elements of the *A*-region in the *x*-direction	100
$n_{y,A}$	Number of elements of the *A*-region in the *y*-direction	100
$l_{x,B}$	Distance between the *A*- and *B*-regions in the *x*-direction	0.25
$l_{y,B}$	Distance between the *A*- and *B*-regions in the *y*-direction	0.25
$n_{x,B}$	Number of elements between the *A*- and *B*-regions in the *x*-direction	25
$n_{y,B}$	Number of elements between the *A*- and *B*-regions in the *y*-direction	25
$l_{x,C}$	Distance between the *B*- and *C*-regions in the *x*-direction	0.25
$l_{y,C}$	Distance between the *B*- and *C*-regions in the *y*-direction	0.25
$n_{x,C}$	Number of elements between the *B*- and *C*-regions in the *x*-direction	7
$n_{y,C}$	Number of elements between the *B*- and *C*-regions in the *y*-direction	7

All the simulations are performed with $\dot{\epsilon} = 0.5$, $\eta = 1.0$, $\Delta t = 0.05$. No artificial repulsive force is implemented because particle collisions hardly occur, when choosing a sufficiently small time step and fine mesh. Anyway, when a collision occurs the particles slightly overlap. The overlapping leads to a single bigger particle with about zero stress inside: the bulk properties are hardly affected from this configuration.[1] Moreover, the particles can also separate again. The contour plots (for $\dot{\epsilon}t = 2.5$) of the magnitude of the velocity vector, pressure and *xx*-component of the stress tensor are depicted in Figs. 16–18, respectively, for a total of 150 equal-sized particles ($R_p = 0.03$). In these pictures, only the *A*-region is shown.

First of all, we can see that the presence of the particles modifies the circular concentric velocity contours that is typical for an unfilled fluid in an elongational flow. Moreover, the strong influence of the hydrodynamic interactions between the particles is clear: the objects, especially at the center of domain, do not follow the streamlines but the motion is modified by the presence of the other particles.

---

[1] We confirmed this by using a repulsion force according to [5]. The overlapping is reduced, as expected, but the bulk stress is hardly affected: the difference is within the statistical fluctuations.
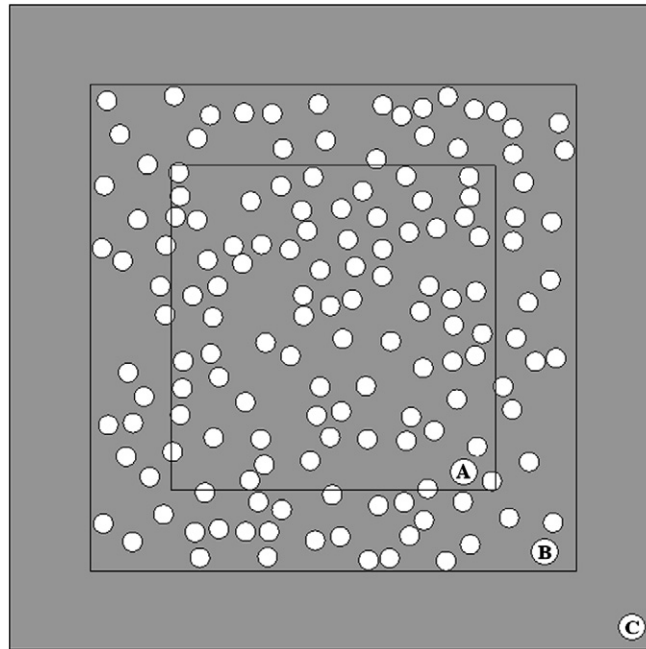
Fig. 15. Initial random distribution of a 150-particle system ($R_p = 0.03$). Only the *A*- and *B*-regions are filled.
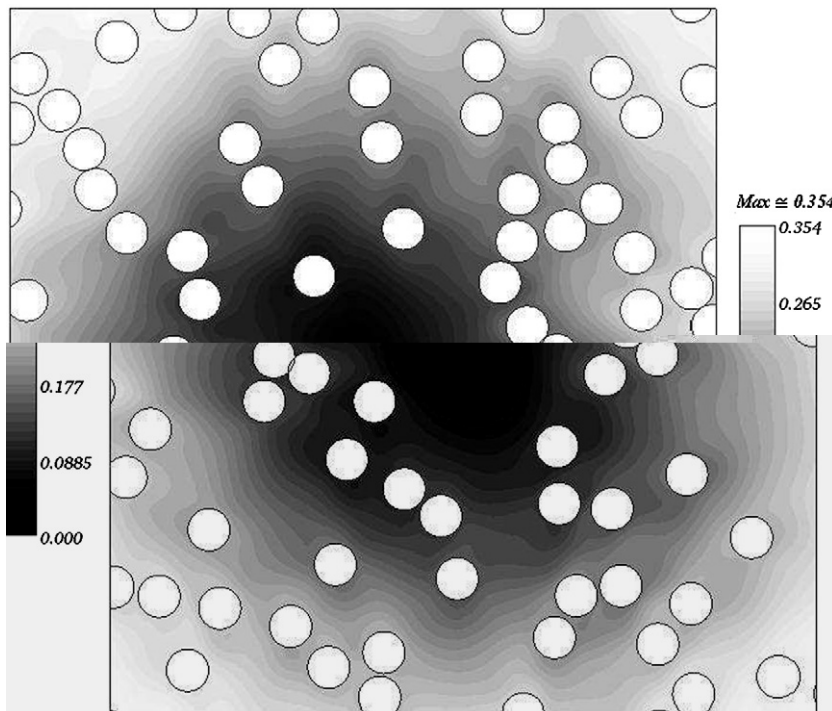

Fig. 16. Contour plot of the velocity magnitude for the 150-particle system ($\dot{\varepsilon}t = 2.5$).

The local pressure field (see Fig. 17) shows the highest values (white zones) along the vertical direction between two particles and the lowest values along the horizontal one (dark regions). This agrees with the dilute theories. Of course, the local stress tensor σ_{xx} (see Fig. 18) shows an opposite behavior. Finally, pressure and
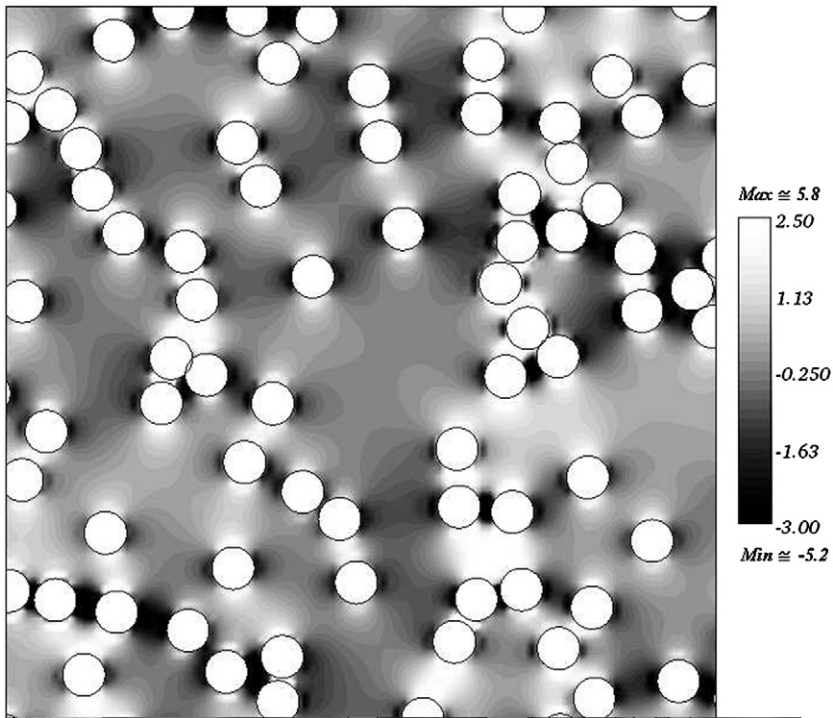
Fig. 17. Contour plot of the pressure for the 150-particle system ($\dot{\epsilon}t = 2.5$).
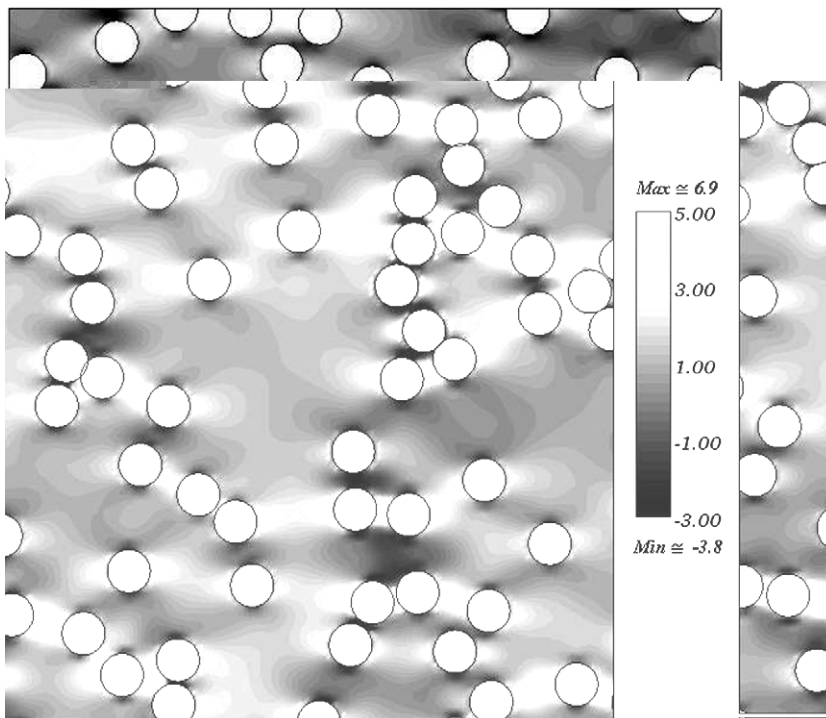

Fig. 18. Contour plot of the xx-component of the stress tensor for the 150-particle system ($\dot{\epsilon}t = 2.5$).

stress are larger in absolute value if the particles are close to each other. This effect leads to an increase of the viscosity with increasing the particle area fraction (see below).

In Fig. 19, the particle area fraction in the A-region versus time is plotted. As mentioned earlier the number of particles in that region is not constant. As a result the particle area fraction is also not constant, but it is a continuous function of time due to the way the particles on the boundary of the A-region are taken into account (see Eq. (27)).

The xx- and yy-components of the bulk stress tensor are shown in Fig. 20. Contrary to the particle area fraction, these functions are discontinuous. The reason can be understood considering the formula for the evaluation of the bulk stress, Eq. (28). When a particle crosses the boundaries of the A-region and the center is outside this region, it does not give a contribution to the bulk stress. As soon as the center of the particle is inside the A-region, the contribution of the particle is immediately taken into account. This leads to a "jump" into the bulk stress components. However, this jump is relatively small because the contribution of only one particle is only a small part of the total stress. Averaging the stress in time will smooth out these jumps.
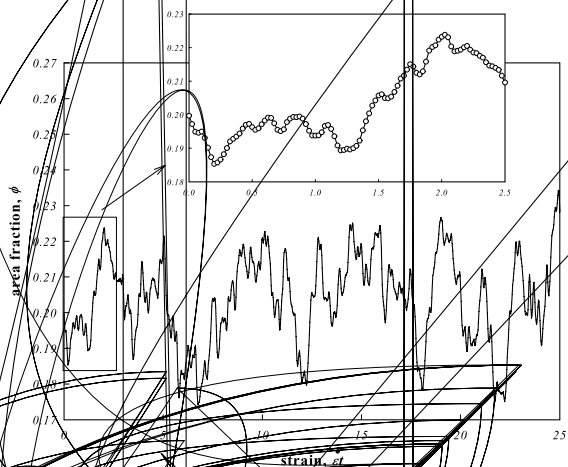

Fig. 19. Particle area fraction as a function of the strain for the 150-particle system and $R_p = 0.03$. The particle area fraction is evaluated only into the A-region where the number of particles is not constant (Eq. (27)). Indeed, $\phi(\dot{\varepsilon}t)$ is a continuous function of the time.
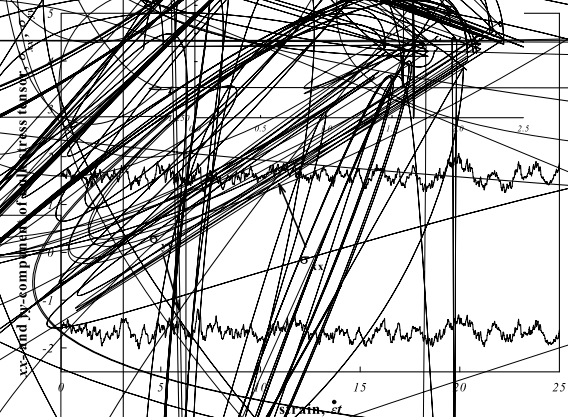
Fig. 20 clearly shows that the two components of the bulk stress fluctuate around a mean value. However, no transient behavior occurs contrarily to the results of Hwang and Hulsen [3].

The average values of the stress components over 2000 time steps are: $\bar{\sigma}_{xx} = 1.603$ and $\bar{\sigma}_{yy} = -1.656$. Hence, a deviation between the absolute values of the average stress components exists (we verified that this discrepancy is independent from the chosen number of the time steps). This suggests the existence of an anisotropic structure, as reported in [3]. In order to verify this anisotropy, we use the same method of [3], by introducing an average horizontal and vertical distance between the two closest particles. The horizontal distance for each particle to the others is defined by considering the horizontal distance to the closest particle within an angular window of $\pm 45°$ about the x-axis. The vertical distance is defined similarly but now using $\pm 45°$ about the y-axis. By evaluating the two distances for every particle and by averaging over the total particle number, the plot in Fig. 21 is obtained. Firstly, no transient phase is observed. Furthermore, the distances fluctuate around two mean values that are 0.111 for the horizontal distance and 0.106 for the vertical one. So, we can conclude that a small anisotropy in the structure exists: the particles are slightly farther apart along the horizontal direction than along the vertical one. Note that our calculations predict an anisotropy less pronounced than in [3] (the deviation between the two average distances is about 4% of their average value whereas it is 14% in [3]).

As expected, the xy-component of the stress tensor (not shown) fluctuates around a mean value that is very close to zero (the fluctuations are about ± 0.03–0.04).
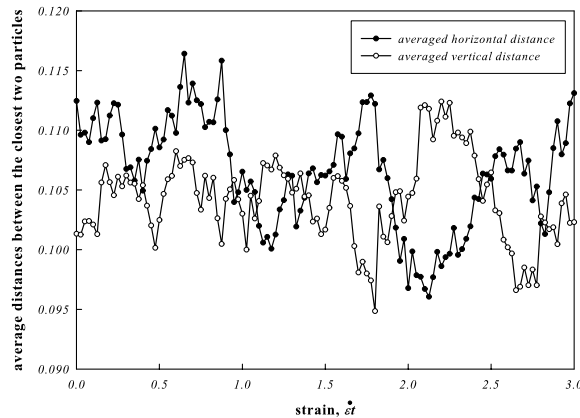

Fig. 21. Average horizontal and vertical distances between the two closest particles as a function of the strain (evaluated according to [3]). Fluctuations around a mean value can be observed and no transient phase occurs.
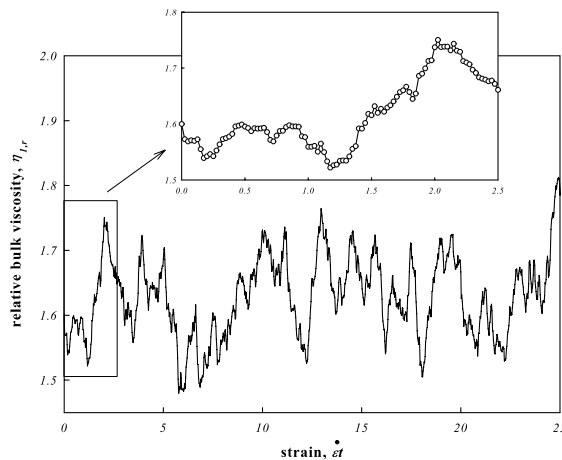

Fig. 22. Relative bulk viscosity as a function of the strain for the 150-particle system. The viscosity is evaluated only in the A-region where the number of particles is not constant (Eq. (29)).

Finally, in Fig. 22, the relative bulk viscosity

$$\eta_{1,r} = \frac{\eta_1}{4\eta_0} = \frac{\sigma_{xx} - \sigma_{yy}}{\dot{\epsilon}_{\mathrm{eff}}} \cdot \frac{1}{4\eta_0} \tag{29}$$

is plotted. In Eq. (29), σ_{xx} and σ_{yy} are the xx- and yy-components of the bulk stress tensor, η_0 is the zero-shear-rate viscosity and $\dot{\epsilon}_{\mathrm{eff}}$ is an effective elongational rate evaluated by performing the integral of $\boldsymbol{D}$ over the A-region for every particle configuration. Of course, $\dot{\epsilon}_{\mathrm{eff}}$ is a function of time since the particle distribution changes each time step. The fluctuations in $\dot{\epsilon}_{\mathrm{eff}}$ are small and the time average value is slightly below the imposed $\dot{\epsilon}$. For example, for $\phi = 0.277$ we find the average value of $\dot{\epsilon}_{\mathrm{eff}} = 0.485$. The factor "4" in Eq. (29) is due to the bi-dimensional Trouton ratio. A similarity between particle area fraction and viscosity trends can be noticed, which confirms what said previously: a higher particle area fraction increases the bulk viscosity.

It is possible to recover the average properties of suspension by averaging over a sufficient high number of configurations (=time steps). In our simulations, 2000 time steps are considered to be enough since the average values do not change anymore. In Fig. 23, the results are shown. In particular, the average relative bulk viscosity:

$$\bar{\eta}_{1,r} = \frac{\bar{\eta}_1}{4\eta_0} = \left\langle \frac{\sigma_{xx} - \sigma_{yy}}{\dot{\epsilon}_{\mathrm{eff}}} \right\rangle \cdot \frac{1}{4\eta_0} \tag{30}$$

versus the average particle area fraction is plotted. The dashed line refers to the well-known Einstein prediction for dilute systems (for the 2D case) [14]:

$$\eta_{\mathrm{Ein}} = \frac{\bar{\eta}_1}{4\eta_0} = 1 + 2\phi \tag{31}$$

that is valid for $\phi \leqslant 0.05$. For higher particle area fractions, hydrodynamic interactions cannot be neglected anymore. The circles represent our predictions for 150 (full circles) and 225 (open circles) particles: each circle corresponds to a simulation and the particle area fraction is varied by changing the particle radius. Strongly dilute systems can be simulated by performing sufficiently long simulations in order to correctly recover the average properties. However, small particle area fractions should be obtained by reducing the number of particles. Since reducing the radius of the particles leads to a too few number of collocation points on the particle boundaries (for $N_p = 225$ and $R_p = 0.02$ we have used $N_c = 12$ that is the lower limit for a good discretization of particle curvature). Therefore, the points for $\phi \cong 0.03$, $\phi \cong 0.054$, $\phi \cong 0.08$ are obtained by considering $N_p = 20$, $N_p = 40$, $N_p = 60$, respectively, and $R_p = 0.03$ (open diamonds). Finally, the solid line is obtained by connecting the viscosities for $N_p = 150$ (full circles) and for the dilute system (open diamonds) with straight lines.
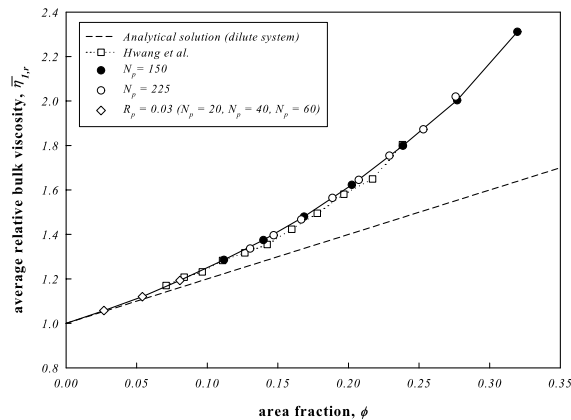

Fig. 23. Relative bulk viscosity as a function of the particle area fraction for a 150-particle (full circles) and 225-particle system (open circles). Hwang and Hulsen results [3] are plotted as well (open squares). The dilute systems are simulated by considering a small number of particles (open diamonds).

Our predictions show an increasing viscosity with increasing the particle area fraction. The trend is not linear but exponential, as found experimentally. The results for 225 particles match the 150 particles ones: 150 particles are sufficient to describe adequately the bulk properties of the suspension. Moreover, for dilute systems, the curve approaches the Einstein solution, as expected.

Finally, in the same figure, a comparison with the results of Hwang and Hulsen [3] is shown (open squares). As we can see, our predicted viscosity curve is slightly above the Hwang and Hulsen one. However, it is important to point out that the viscosities reported by Hwang and Hulsen refer to the initial random distribution of the particles in the bi-periodic domain and they found an increasing transient behavior in time (which our simulations do not predict). Considering the uncertainty in the steady state value in their results we think the agreement is very good.

8. Conclusions

In this work, a new simulation scheme for direct simulation of concentrated particle suspensions has been presented and implemented. Our simulation scheme is based on a three-layer domain that is able to: (i) consider a small domain as a sample of the suspension, (ii) impose the planar elongational flow boundary conditions sufficiently far from the particles and (iii) calculate the steady state properties (in a statistical meaning) of the suspension. We do not need to deform the computational domain and no periodic boundary condition is imposed as in [3].

A steady state can be achieved by relocating the particles on the inflow sections when they cross the outflow sides of the domain.

We used a fictitious domain that is able to easily manage the rigid-body motion of the particles and to evaluate directly the hydrodynamic interactions, without approximations. So, we can obtain a combined weak formulation of the particle and fluid domain. This weak form has been discretized through a finite element method. The advantages of this procedure are: (i) a time-independent mesh can be used, (ii) the particle domain is discretized through the particle boundaries only (rigid-ring description) and (iii) the rigid-body motion constraints are imposed by means the Lagrange multipliers (that are related to the traction force on the particle boundaries).

In order to demonstrate the feasibility of our method, we performed 2D simulations with an high number of the particles (150 and 225) in order to recover the bulk properties of a Newtonian suspension, by neglecting the fluid and particle inertia.

The local distribution of the flow and stress fields as well as the bulk properties are evaluated. These last ones are related to the bulk stress calculated through the Batchelor formula [7] where a particle and a fluid contribution are taken into account.

The results showed a very good agreement with dilute theory as well as other numerical simulations in the literature. In particular, for low particle area fractions, the relative bulk viscosity approaches the Einstein's analytical solution. By increasing the area fraction, the viscosity increases as well according to an exponential-like trend, as shown in the experiments. For concentrated systems, our results agree with the results of Hwang and Hulsen [3], obtained by using a different scheme. Finally, as in [3], we found an anisotropic structure where the particles are slightly farther apart along the horizontal direction than along the vertical direction. However, according to our calculations, the anisotropy is less pronounced than in [3]. Moreover, we do not observe any start-up phase.

Our scheme can be easily extended to 3D problems as well as to suspensions of viscoelastic fluids. In particular, to circumvent the memory limitations in 3D simulations, iterative solvers and parallel calculations will be required.

References

[1] W. Hwang, M. Hulsen, H. Meijer, Direct simulation of particle suspensions in sliding bi-periodic frames, J. Comput. Phys. 194 (2004) 742.
[2] W. Hwang, M. Hulsen, H. Meijer, Direct simulation of particle suspensions in a viscoelastic fluid in sliding bi-periodic frames, J. Non-Newtonian Fluid Mech. 121 (2004) 15.

[3] W. Hwang, M. Hulsen, Direct numerical simulations of hard particle suspensions in planar elongational flow, J. Non-Newtonian Fluid Mech. 136 (2006) 167.

[4] J. Brady, G. Bossis, Stokesian dynamics, Ann. Rev. Fluid Mech. 20 (1988) 111.

[5] R. Glowinski, T.-W. Pan, D.J.T.I. Hesla, A distributed Lagrangian multipliers/fictitious domain method for particulate flows, Int. J. Multiphase Flow 25 (1999) 755.

[6] F. Bertrand, P. Tanguy, F. Thibault, A three-dimensional fictitious domain method for incompressible fluid flow problems, Int. J. Numer. Meth. Fluids 25 (1997) 719–736.

[7] G. Batchelor, The stress system in a suspension of force-free particles, J. Fluid Mech. 41 (1970) 545.

[8] H. Hu, Direct simulation of flows of solid–liquid mixtures, Int. J. Multiphase Flow 22 (1996) 335.

[9] H. Hu, D. Joseph, M. Crochet, Direct simulation of fluid particle motions, Theor. Comp. Fluid Dyn. 3 (1992) 285.

[10] N. Patankar, Numerical simulation of particulate two-phase flow, Ph.D. Thesis, University of Pennsylvania, Pennsylvania, 1997.

[11] A. Johnson, T. Tezduyar, 3D simulation of fluid–particle interactions with the number of particles reaching 100, Research Report 96-037, Army High Performance Computing Research Center, University of Minnesota, 1996.

[12] HSL, A collection of Fortran codes for large scale scientific computation, 2002. Available from: <http://www.cse.clrc.ac.uk/nag/hsl/>.

[13] F. Baaijens, A fictitious domain/mortar element method for fluid–structure interaction, J. Non-Newtonian Fluid Mech. 79 (1998) 361.

[14] A. Einstein, Berichtigung zu Meiner Arbeiten: Eine Neue Bestimmung der Molekul Dimensionen, Ann. Phys. Berlin 19 (1906) 289.